2020-09

EFFECTS OF INTERNAL HEATING ON THE DYNAMICS AND PATTERNS OF STRATIFIED WAKES

Huang, Lianghai C.

Monterey, CA; Naval Postgraduate School

NAVAL POSTGRADUATE SCHOOL

MONTEREY, CALIFORNIA

THESIS

EFFECTS OF INTERNAL HEATING ON THE DYNAMICS AND PATTERNS OF STRATIFIED WAKES

by

Lianghai C. Huang

September 2020

Thesis Advisor: Timour Radko
Second Reader: Justin M. Brown

Approved for public release. Distribution is unlimited.

THIS PAGE INTENTIONALLY LEFT BLANK

REPORT DOCUMENTATION PAGE			*Form Approved OMB No. 0704-0188*

1. AGENCY USE ONLY *(Leave blank)*	**2. REPORT DATE** September 2020	**3. REPORT TYPE AND DATES COVERED** Master's thesis

4. TITLE AND SUBTITLE EFFECTS OF INTERNAL HEATING ON THE DYNAMICS AND PATTERNS OF STRATIFIED WAKES	**5. FUNDING NUMBERS**
6. AUTHOR(S) Lianghai C. Huang	
7. PERFORMING ORGANIZATION NAME(S) AND ADDRESS(ES) Naval Postgraduate School Monterey, CA 93943-5000	**8. PERFORMING ORGANIZATION REPORT NUMBER**
9. SPONSORING / MONITORING AGENCY NAME(S) AND ADDRESS(ES) N/A	**10. SPONSORING / MONITORING AGENCY REPORT NUMBER**

11. SUPPLEMENTARY NOTES The views expressed in this thesis are those of the author and do not reflect the official policy or position of the Department of Defense or the U.S. Government.

12a. DISTRIBUTION / AVAILABILITY STATEMENT Approved for public release. Distribution is unlimited.	**12b. DISTRIBUTION CODE** A

13. ABSTRACT (maximum 200 words)

With advancing technology, submarines are getting quieter, and detection methods may need to include non-acoustical means. Wake detection is one such method that can be used for submarine detection. An internally heated submerged body such as a submarine travelling through stratified ocean columns generates a warm wake. Using the Massachusetts Institute of Technology General Circulation Model (MITgcm), we conducted a series of large eddy simulations to model the quantitative and qualitative effects of the warm wake produced by a towed spherical submerged body with a heating source. In this study, we studied the effects of varying the heating rate and noted that there are observable differences in the thermal anomaly between these cases during the early wake. At later times, heating of the wake does not seem to have a substantial effect on the thermal and turbulent characteristics of the wake. Distinctive loop shapes form in slices of the turbulent dissipation rate in all cases that may be used to easily identify submarine wakes. We also observed that the thermal anomaly is correlated to the submerged body's velocity and to higher background salinity gradients for comparable density stratification.

14. SUBJECT TERMS stratified wake, internal heating, propagating, detection, Massachusetts Institute of Technology General Circulation Model, MITgcm	**15. NUMBER OF PAGES** 49
	16. PRICE CODE

17. SECURITY CLASSIFICATION OF REPORT	**18. SECURITY CLASSIFICATION OF THIS PAGE**	**19. SECURITY CLASSIFICATION OF ABSTRACT**	**20. LIMITATION OF ABSTRACT**
Unclassified	Unclassified	Unclassified	UU

NSN 7540-01-280-5500

Standard Form 298 (Rev. 2-89)
Prescribed by ANSI Std. 239-18

THIS PAGE INTENTIONALLY LEFT BLANK

Approved for public release. Distribution is unlimited.

EFFECTS OF INTERNAL HEATING ON THE DYNAMICS AND PATTERNS OF STRATIFIED WAKES

Lianghai C. Huang
Major, Republic of Singapore Navy
Bachelor of Engineering (Environmental Engineering), Nanyang Technological University, 2009

Submitted in partial fulfillment of the
requirements for the degree of

MASTER OF SCIENCE IN PHYSICAL OCEANOGRAPHY

from the

NAVAL POSTGRADUATE SCHOOL
September 2020

Approved by: Timour Radko
Advisor

Justin M. Brown
Second Reader

Peter C. Chu
Chair, Department of Oceanography

THIS PAGE INTENTIONALLY LEFT BLANK

ABSTRACT

With advancing technology, submarines are getting quieter, and detection methods may need to include non-acoustical means. Wake detection is one such method that can be used for submarine detection. An internally heated submerged body such as a submarine travelling through stratified ocean columns generates a warm wake. Using the Massachusetts Institute of Technology General Circulation Model (MITgcm), we conducted a series of large eddy simulations to model the quantitative and qualitative effects of the warm wake produced by a towed spherical submerged body with a heating source. In this study, we studied the effects of varying the heating rate and noted that there are observable differences in the thermal anomaly between these cases during the early wake. At later times, heating of the wake does not seem to have a substantial effect on the thermal and turbulent characteristics of the wake. Distinctive loop shapes form in slices of the turbulent dissipation rate in all cases that may be used to easily identify submarine wakes. We also observed that the thermal anomaly is correlated to the submerged body's velocity and to higher background salinity gradients for comparable density stratification.

THIS PAGE INTENTIONALLY LEFT BLANK

TABLE OF CONTENTS

I. INTRODUCTION....1
- **A. MOTIVATION....1**
- **B. BACKGROUND....1**

II. METHODS....5
- **A. GOVERNING EQUATIONS....5**
- **B. COMPUTATIONAL CONFIGURATION....5**
- **C. SUBMERGED BODY....6**

III. RESULTS....9
- **A. WAKE STRUCTURE AND MORPHOLOGY....9**
  - **1. Heating Rate....9**
  - **2. SB Velocity....11**
  - **3. Background Salinity Field....15**
- **B. DISSIPATION RATES....18**

IV. DISCUSSION....25
- **A. CONCLUSION....25**
- **B. OPERATIONAL RELEVANCE....26**
- **C. FUTURE RESEARCH....27**

LIST OF REFERENCES....29

INITIAL DISTRIBUTION LIST....31

THIS PAGE INTENTIONALLY LEFT BLANK

LIST OF FIGURES

Figure 1. Model configuration: grid-spacing, resolution, and boundary conditions. 7

Figure 2. 3D model output at time of 400s showing the velocity perturbation of the heated wake 8

Figure 3. Plot of the maximum T' vs *Nt* for the varying *Q* runs. 10

Figure 4. The left column shows the *xz*-plane while the right column shows the *yz*-plane through the entire domain taken at $y = 100$ and $x = 500$, respectively. The top, middle and bottom rows are for Nt ~1, 5 and 20, respectively, observed at for $Q = 2.2 \times 10^9$W 11

Figure 5. The top plot shows the maximum T' as a function of non-dimensional time, *Nt*, while the bottom plot compares the RMS T' as a function of non-dimensional time for various u_0 13

Figure 6. The left column shows the *xz*-plane while the right column shows the *yz*-plane through the entire domain taken at $y = 100$ and $x = 500$, respectively. The top, middle and bottom row are for u_0 of 2.5m/s, 5.0m/s and 10.0m/s, respectively, observed at $Nt \sim 1$ 14

Figure 7. The left column shows the *xz*-plane while the right column shows the *yz*-plane through the entire domain taken at $y = 100$ and $x = 500$, respectively. The top, middle and bottom rows are for u_0 of 2.5m/s, 5.0m/s and 10.0m/s, respectively, observed at $Nt \sim 5$ 14

Figure 8. The left column shows the *xz*-plane while the right column shows the *yz*-plane through the entire domain taken at $y = 100$ and $x = 500$, respectively. The top, middle and bottom rows are for u_0 of 2.5m/s, 5.0m/s and 10.0m/s, respectively, observed at $Nt \sim 20$ 15

Figure 9. The top plot shows the maximum T' as a function of non-dimensional time, *Nt*, while the bottom plot compares the RMS T' as a function of non-dimensional time for various $\partial S \partial z$ runs. 17

Figure 10. The left column shows the *xz*-plane while the right column shows the *yz*-plane through the entire domain taken at $y = 100$ and $x = 500$, respectively. The top, middle and bottom rows are for $\partial S \partial z$ of 0.000 PSU/m, 0.007 PSU/m and 0.014 PSU/m, respectively, observed at $Nt \sim 5$ 18

Figure 11. The left, middle and right column show the *x*-averaged ε taken at *Nt* ~ 1, 5, and 20, respectively. The top, middle and bottom rows are for *Q* of 0W, 2.2×10^9W and 4.4×10^9W, respectively. The height and width of the region with elevated ε is shown in bottom right of each plot. 20

Figure 12. The left and right column show slices of ε taken at *Nt* ~ 5, and 20, respectively. The top, middle and bottom rows are for *Q* of 0W, 2.2×10^9W and 4.4×10^9W, respectively.....21

Figure 13. The left and right column show the ε taken at *Nt* ~ 5 and *Nt* ~ 20, respectively. The top, middle and bottom rows are for u_0 of 2.5m/s, 5.0m/s and 10m/s, respectively. The height and width of the area with elevated ε is shown in bottom right of each plot. 23

Figure 14. The left and right column show the ε taken at Nt ~ 5 and Nt ~ 20, respectively. The top, middle and bottom rows are for $\partial S \partial z$ of 0.000 PSU/m, 0.007 PSU/m and 0.014 PSU/m, respectively. The height and width of the area with high ε is shown in bottom right of each plot. 24

LIST OF TABLES

Table 1. List of simulations.....8

THIS PAGE INTENTIONALLY LEFT BLANK

LIST OF ACRONYMS AND ABBREVIATIONS

ASW	Anti-submarine warfare
DNS	Direct numerical simulation
Fr	Froude number
LES	large eddy simulation
MITgcm	Massachusetts Institute of Technology General Circulation Model
PSU	Practical Salinity Unit
Re	Reynolds number
RMS	root mean square
SB	submerged body

THIS PAGE INTENTIONALLY LEFT BLANK

ACKNOWLEDGMENTS

I would like to thank my wonderful thesis advisor, Professor Timour Radko, for introducing me to this field of research. Never would I have thought that I would be using simulations to advance my knowledge in this field of studies. Thank you for your patience and motivation throughout these times.

These simulations would not have been possible if not for the intense coaching by Dr Justin Brown. His deep expertise in MITgcm and superbly clear instructions allowed me to grasp the knowledge of the model in double-quick time, especially in this special period of distance learning. Thank you for always being there to troubleshoot my simulations. Without you, I would not have been able to complete this study on time.

Thank you to all the friends that I have made in my journey throughout NPS. There's no way I could name all of you. Your little acts of kindness have surely impacted me in one way or another.

Lastly, I would like to thank my wife, Jolene, for sacrificing her career in order to move to Monterey to allow me to pursue my master's degree in NPS. Thank you for taking care of our lovely son, Jayce.

THIS PAGE INTENTIONALLY LEFT BLANK

I. INTRODUCTION

A. MOTIVATION

Detecting submarines requires navies to constantly improve undersea detection technologies, using new sensor platforms—such as satellites and unmanned underwater vehicles—and new detection methods, including those that do not rely on direct acoustical measurement. One such method that has shown promise as an alternative method for submarine detection is the use of wake turbulence (Voropayev et al., 1999). Instead of measuring the acoustic signatures of submarine machinery or responses to active sonar, the wake caused by the traversing submarine can be detected via acoustic and non-acoustic methods, including visual, thermal, and radar-based means. This form of submarine detection can theoretically counter submarine acoustic nose reduction.

When a submerged body (SB) travels through a stratified fluid at substantial velocity, a turbulent wake is produced. This wake may be detectable either by direct measurements of turbulence, including measurements of velocity at small scales, or indirect measurements via the turbulent dissipation rate and temperature signatures. The subject of thermal wakes has received only limited coverage in the current literature (see, for example, Zhang et al., 2019). Vital machinery aboard a submarine emits heat during operation, which necessitates cooling, often using seawater. After its use, the seawater is returned to the ocean. The nuclear reactor on a submarine generates heat used to drive propulsion, and the excess heat is typically discharged into the submarine wake. This heated discharge will form a thermal wake with a temperature higher than that of the surrounding seawater. We address the topic of whether the warm submarine wakes might have specific signatures that could be utilized in wake detection. Hence, this study seeks to advance the current understanding of wake behaviors, with special focus on heated wakes.

B. BACKGROUND

This fluid flow at various scales can be commonly described in terms of dimensionless parameters such as the Reynolds number (Re) and the Froude number (Fr).

The Reynolds number describes the ratio of inertial forces to viscous forces within a fluid and is defined as

$$Re = \frac{UL}{\upsilon}, \tag{1.1}$$

where U is the speed of the SB, L is the length scale of the SB, and υ is the kinematic viscosity. When Re increases above a critical value (typically 5000), wakes generated by a moving SB in a stratified fluid become turbulent, whereas at small Re, viscous forces dominate, which results in a laminar flow.

Stratified flows are also characterized by the Froude number, defined as the ratio of inertial forces to buoyancy:

$$Fr = \frac{U}{NL}, \tag{1.2}$$

where N is the Brunt-Väisälä or buoyancy frequency, defined as

$$N = \sqrt{-\frac{g}{\rho_0}\frac{\partial \rho}{\partial z}}, \tag{1.3}$$

where g is the gravitational acceleration, ρ_0 is a reference density, and ρ is the density of the fluid. As Fr becomes much larger than unity, the effects of buoyancy become negligible, so Re is the only important number for determining the properties of the flow. In such cases, detections of wake signatures are limited only to velocity signatures and can diffuse rapidly (Schooley and Stewart, 1963). When Fr is small, the effects of buoyancy are strong, which results in substantial changes in the behavior of the intermediate and late wakes.

Wakes created by an SB traversing in a stratified fluid typically have three stages: the near wake, the non-equilibrium wake, and the quasi-two-dimensional wake (Spedding, 1997). The duration of these stages corresponds to the number of buoyancy cycles that have elapsed since the object passed, which is proportional to Nt, where t is the time since passage. The near wake occurs immediately behind the SB ($Nt < 2$), and it mixes the fluid in a cone until it takes on nearly homogenous density (Hopfinger et al., 1991). The vertical

mixing of the wake results in regions of fluid above (below) the level of the SB that is heavier (lighter) than the surrounding fluid at the same depth, which buoyancy will begin to collapse. As the fluid migrates to a depth where it is neutrally buoyant, the wake flattens and expands horizontally. This marks the beginning of the non-equilibrium phase where the turbulence in the wake generates internal waves which radiate outward from the core of the wake itself. Lastly, after the wake has fully collapsed ($Nt > 50$), it enters the quasi-two-dimensional regime, where the vertical velocity component is very small as compared to the horizontal components and expands slowly in height and width (Lin and Pao, 1979).

There have been many studies to date attempting to detect the wakes of submerged objects both in the ocean and in laboratory settings. One such study by Fiekas (1997) measured the temperature distribution across the submarine wake using a towed array of sensors and recorded temperature anomalies of $\sim$0.5°C after the submarine travelled a distance of 1.5km. However, in situ measurements are not the only method of detection, as Voropayev et al. (2007) found in their laboratory studies that an SB could produce measurable signals at the sea surface under the right conditions. These findings further motivate the development of new detection algorithms that are based on thermal signatures of stratified wakes.

Other than conducting physical experiments in the laboratory and taking measurements in the ocean, numerical methods using supercomputers are also used to advance the understanding of this field. One of the many numerical methods is the use of Large Eddy Simulations (LES) as the viscous scale remains beyond our current computing ability to resolve for the scales of interest here. The method of LES allows for focused and quantitative studies of wakes. The study presented in this thesis examines the turbulent structure of a thermal wake using varying physical properties of an SB as well as oceanographic properties as the primary controlling parameters. Using LES of a sphere trailing a warm wake, we investigate the persistence of the temperature and vorticity signatures.

This thesis is organized as follows. Section II describes the model configuration and assumptions. Section III presents the results of the thermal and energy-based

diagnostics. Lastly, Section IV provides conclusions, operational relevance and future research opportunities of the study.

II. METHODS

A. GOVERNING EQUATIONS

All the simulations conducted in this study assume that the system satisfies the Boussinesq approximation and does not experience external rotation. We simulate fluid flows by solving the Navier-Stokes equations under these assumptions, which are given by

$$\nabla \cdot \boldsymbol{u} = 0, \tag{2.1}$$

$$\frac{\partial T}{\partial t} + \boldsymbol{u} \cdot \nabla T = \kappa_T \nabla^2 T + \frac{Q}{\rho_0 C_p}, \tag{2.2}$$

$$\frac{\partial S}{\partial t} + \boldsymbol{u} \cdot \nabla S = \kappa_S \nabla^2 S, \tag{2.3}$$

$$\rho_0 \left(\frac{\partial \boldsymbol{u}}{\partial t} + \boldsymbol{u} \cdot \nabla \boldsymbol{u} \right) = -\nabla p + \rho_0 [-\alpha (T - T_0) + \beta (S - S_0)] \boldsymbol{g} + \rho_0 \upsilon \nabla^2 \boldsymbol{u}, \tag{2.4}$$

where **u** is the velocity, T is the temperature, t is time, κ_T and κ_S are the temperature and salinity diffusivities, respectively, Q is the heat source in the wake, C_p is the specific heat capacity of water, S is the salinity, p is the pressure, α is the coefficient of thermal expansion, β is the coefficient of haline contraction, **g** is the gravitational acceleration, and T_0 and S_0 are the reference values of temperature and salinity, respectively.

B. COMPUTATIONAL CONFIGURATION

We used the Massachusetts Institute of Technology General Circulation Model (MITgcm) to conduct the numerical simulations of this study. It is a non-hydrostatic ocean model that is able to resolve small-scale features efficiently through parallel processing (Marshall et al., 1997). One of the key features of MITgcm is that its algorithm can solve the incompressible Navier-Stokes equations over a broad range of scales.

The wake was resolved with 200 grid points spaced exponentially along the *y* and *z* directions in order to resolve the fine-scale features of the wake at the level of the SB.

At the vicinity of the SB, the resolution was the highest— $\min(\Delta y) = \min(\Delta z) = 0.5\text{m}$ —and the grid spacing was exponentially increased to $\max(\Delta y) = \max(\Delta z) = 3.5513\text{m}$ at the edges of the computational domain. The *x* direction was uniformly resolved with 1920 grid points spaced at $\Delta x = 0.5\text{m}$. The periodic boundary conditions were applied at sidewalls, which have been sufficiently separated to prevent their influence on the interior wake. The top and bottom are modelled by a free surface and an impermeable boundary, respectively. We model the mixing by eddies smaller than the grid scale of this simulation using constant eddy viscosity and eddy diffusivity. In accordance with the Reynolds analogy, we assume that the eddy dissipation of momentum and the temperature/salinity fields are comparable. The fluid is at rest until acted upon by the SB. The background temperature field and salinity field are given by $\bar{T}(z) = \frac{\partial \bar{T}}{\partial z} z$ and $\bar{S}(z) = \frac{\partial \bar{S}}{\partial z} z$, where both $\frac{\partial \bar{T}}{\partial z}$ and $\frac{\partial \bar{S}}{\partial z}$ are constants, which will be varied in the simulations. The viscosity and the diffusivities of temperature and salinity were set to the uniform values of $\nu = \kappa_T = \kappa_S = 2 \times 10^{-2}\ \text{m}^2/\text{s}$ for both horizontal and vertical dissipation. The value of α and β were $2 \times 10^{-4} °\text{C}^{-1}$ and $7.5 \times 10^{-4} \text{PSU}^{-1}$, respectively. The time step is limited by the Courant–Friedrichs–Levy condition.

C. SUBMERGED BODY

We model a submarine with heated discharge as an impermeable sphere of radius 5m inside our domain that is followed at distance of 40m by a sphere of the same size that is uniformly heated at a rate of *Q*. A sphere was chosen for the SB due to its simplicity and due to the broad coverage of literature on wakes behind spherical objects. The number of model grid points, resolutions, and SB parameters as well as boundary conditions are depicted in Figure 1.

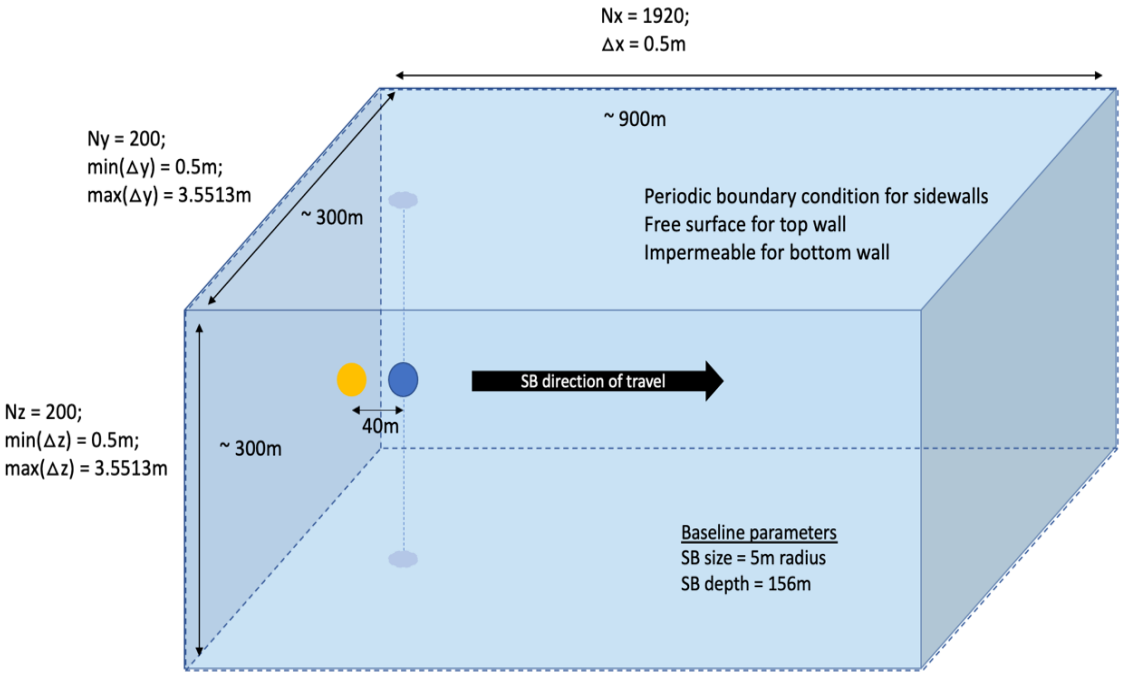

Figure 1. Model configuration: grid-spacing, resolution, and boundary conditions.

At the start of the simulation, the center of the SB is placed at $x = 0$m, 50m away from the boundary ($x = -50$m), to avoid any interference between the wake and the boundary. The SB then travels horizontally along the *x* axis through the center of the box at constant velocity u_0. A 3D model output of the submerged wake is provided in Figure 2. All simulations are summarized in Table 1.

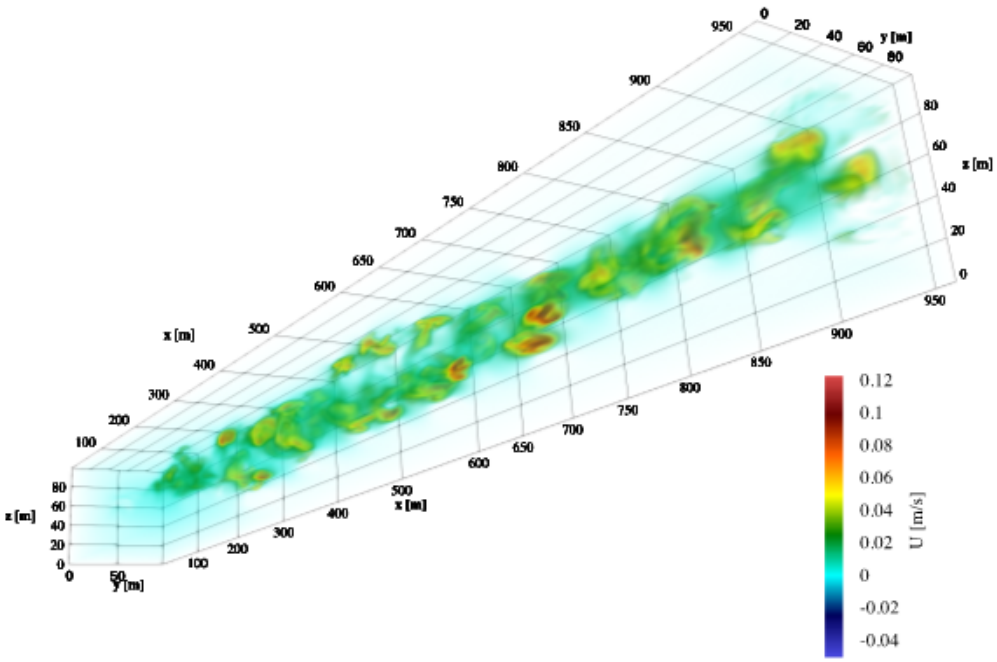

Figure 2. 3D model output at time of 400s showing the velocity perturbation of the heated wake

Table 1. List of simulations

Simulation Run Number	Velocity of SB (m/s)	Temperature Gradient (°C/m)	Salinity Gradient (PSU/m)	Heat Supplied by SB (Watts)	Time Step Δt (s)
1	5	0.03	0.007	1.1×10^9	0.025
2	2.5	0.03	0.007	1.1×10^9	0.025
3	10	0.03	0.007	1.1×10^9	0.010
4	5	0.03	0.007	0	0.025
5	5	0.03	0.007	2.2×10^9	0.025
6	5	0.03	0.007	4.4×10^9	0.025
7	5	0.00375	0.000	1.1×10^9	0.025
8	5	0.05625	0.014	1.1×10^9	0.025

III. RESULTS

This study explores the effects of three parameters controlling the heated wake structure – the heating rate behind the SB (Q), the velocity of the SB (u_0), and the salinity gradient of the water column $\left(\frac{\partial \bar{S}}{\partial z}\right)$. Only one control parameter was varied in each set of simulations while all the other parameters were held constant. This systematic approach allows us to characterize the effects of each parameter on the resultant heated wake signature.

A. WAKE STRUCTURE AND MORPHOLOGY

1. Heating Rate

The first control parameter varied in these simulations was the heating rate, Q. As Q varied, u_0 and $\frac{\partial \bar{S}}{\partial z}$ were held constant at 5.0m/s and 0.007PSU/m, respectively. The wake structures of four different heating rates were investigated: no heating, $Q = 1.1 \times 10^9$W, $Q = 2.2 \times 10^9$W and $Q = 4.4 \times 10^9$W. Figure 3 shows the maximum of the absolute value of the temperature perturbation, $T' \equiv T - \bar{T}$, plotted against non-dimensional time, Nt. At $Nt \sim 1$, both the case without heating and the case with $Q = 2.2 \times 10^9$W achieve comparable local maxima. While the heated case reaches this local maximum as early as $Nt \sim 0.2$, the case without heating takes substantially longer to reach the same value. We attribute this to the heating introduced by the SB moving through the fluid. In the case without heating, the only source of temperature perturbation comes from mixing, which delays this local maximum. The temperature perturbation plateaus at $Nt \sim 0.25$ because the SB leaves the domain and thus the direct heating ends. It appears that the temperature perturbation levels off in all cases after $Nt \sim 0.25$, but by $Nt \sim 1$, they all relax to the same value because of the joint effects of the rising of the warm regions to the level of neutral buoyancy and the turbulent mixing of temperature. We observe that after $Nt \sim 1$, there aren't substantial differences between the three cases. This could be due to the fluid parcels being reasonably close to the level of neutral density, and thus, the thermal perturbation is low.

We plot the thermal perturbation away from the background in Figure 4 for the case of $Q = 2.2 \times 10^9$W at $Nt \sim 1$, 5 and 20. The other two cases look largely identical and thus will not be discussed in detail. In the near wake after the SB has passed, the fluid has reached the level of neutral buoyancy, but there is still obvious turbulence that is actively mixing the core of the wake. As the wake develops, the perturbation in the core is lost to the turbulent diffusion of temperature and is also radiated away in the form of internal waves—the latter effect is visibly evident in the $Nt \sim 5$ plot. This results in the decay of the temperature perturbation as seen in Figure 3. By $Nt \sim 20$, all the thermal variance in the core of the wake has been dissipated by these processes, and the only remaining evidence of the wake in the temperature is in the lingering internal waves. Because there is no appreciable difference in thermal perturbation in morphology or magnitude after $Nt \sim 1$, it seems unlikely that the effects of wake heating will substantially affect typical wake signatures at late times. However, it may still alter the effects of other factors that affect wake structure.

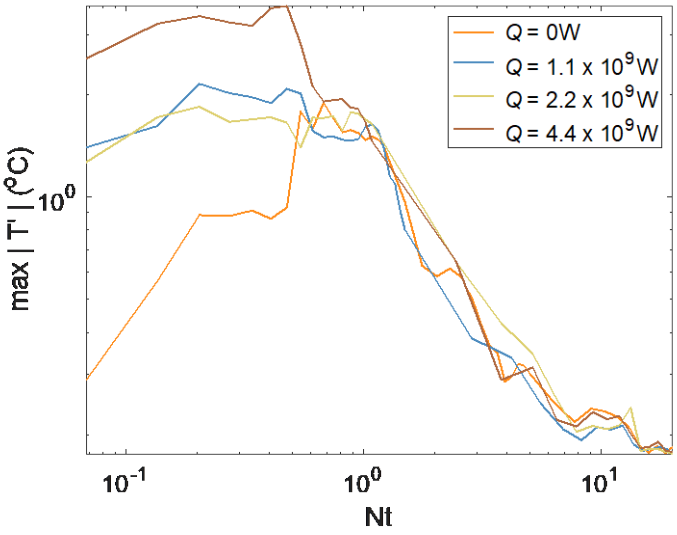

Figure 3. Plot of the maximum $|T'|$ vs Nt for the varying Q runs.

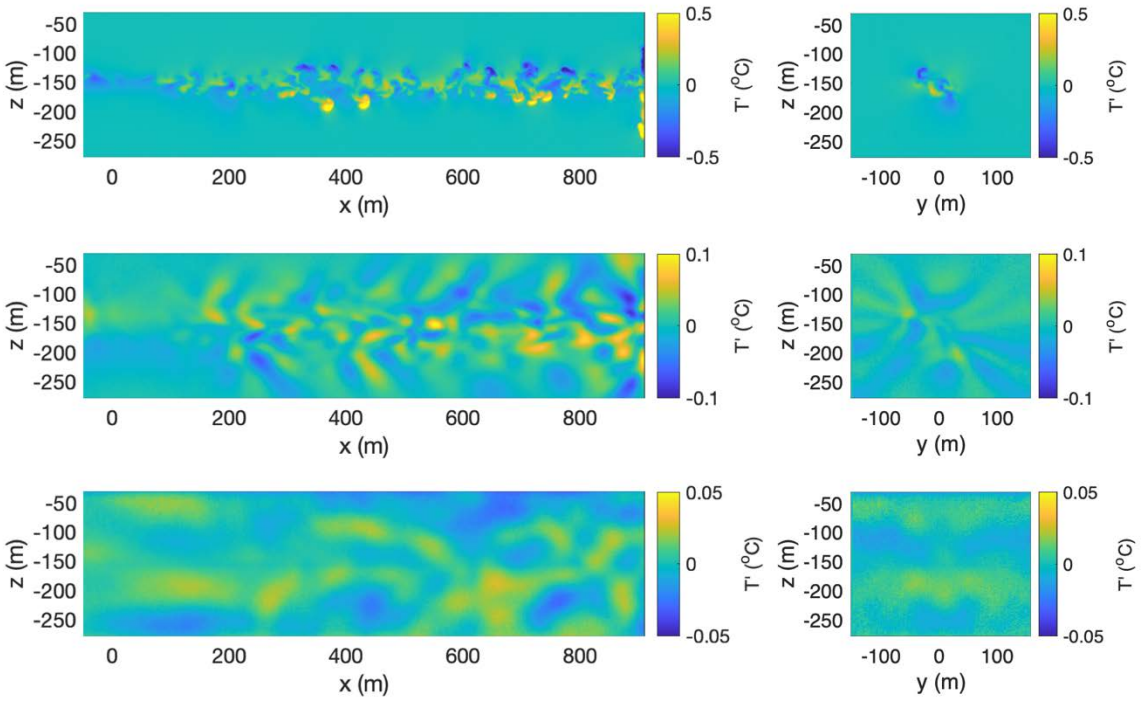

Figure 4. The left column shows the *xz*-plane while the right column shows the *yz*-plane through the entire domain taken at $y = 100$ and $x = 500$, respectively. The top, middle and bottom rows are for Nt ~1, 5 and 20, respectively, observed at for $Q = 2.2 \times 10^9$W

2. SB Velocity

The second control parameter varied in these simulations was the velocity of the SB. As u_0 varied, $\frac{\partial \bar{s}}{\partial z}$ and Q were held constant at 0.007 PSU/m and 1.1×10^9W, respectively. For these simulations, we examine both the maximum $|T'|$ as well as the root mean square (RMS) of $|T'|$ as functions of non-dimensional time in Figure 5. The maximum $|T'|$ for all three cases reach a local maximum between $Nt \sim 0.2$ and 0.4. These large values are due to the heating of the SB. The maximum of $|T'|$ starts highest for the slowest case, which can be attributed to longer sustained heating for a given Q, but this case also sees the fastest decay of this measure. This is probably due to the reduced amount of turbulence as compared to the other two cases, leading to less mixing in the SB wake.

Looking at the RMS of $|T'|$, a peak occurs in all three cases at $Nt \sim 1$, and the fastest case shows the largest RMS value. This is due to the fastest case producing the greatest amount of turbulence, which results in large local deviations from the mean temperature field. We observe the smallest peak for the u_0 = 2.5m/s case. Therefore, we can conclude that a SB with low velocity could be readily detected using temperature anomaly at early times, but the wake becomes difficult to discern more rapidly than is the case for faster moving objects.

Figure 6 shows the temperature perturbation field at $Nt \sim 1$ for the three simulations with varying SB velocities: 2.5m/s, 5.0m/s and 10.0m/s. For the case of u_0 = 2.5m/s, we observe a tilt in the wake track and a warm region in the front that has not yet risen to neutral buoyancy. This horizontal heterogeneity is not present in the two cases with higher Reynolds number. Additionally, there is substantially more small-scale structure and larger apparent velocities in the u_0 = 10.0m/s case due to the higher Re of the flow, which will result in more turbulent mixing and larger physical extents of the turbulent wake core in the later stages.

Figure 7 shows the temperature perturbation approximately twenty-five minutes later ($Nt \sim 5$), which evolves analogously to the case in Section III.A.1. The wake core is most compact for the u_0 = 2.5m/s case, and the core gets larger at higher velocities. This is a direct consequence of the higher Re flows producing more turbulence and therefore inducing more turbulent mixing (which is indirectly evidenced by the higher plumes in the bottom panels of Figure 6). We also observe that the internal waves themselves have their largest amplitudes in the u_0 = 10.0m/s case because they are produced from stronger turbulence. In addition, the core of the u_0 = 10.0m/s case is observed to have flattened in agreement with the description of wake evolution in Section I. This behavior is only evident in the u_0 = 10.0m/s case, which may be due to an insufficient amount of vertical mixing in the lower Re cases. In Figure 8, we examine the temperature perturbation approximately two hours ($Nt \sim 20$) after the SB has passed. The wake signal has substantially dissipated in all three velocity profiles leaving pockets of strong temperature perturbation within the domain. In the *y*–*z* plane, we observe that the turbulent core has almost dissipated completely, leaving a concentration of internal waves near the location of the SB path;

however, distinguishing these from ambient waves in the ocean might prove exceptionally difficult. From these three simulations, it appears the wake heating only matters at early times, and it seems to be less important to the wake dynamics than the Reynolds number.

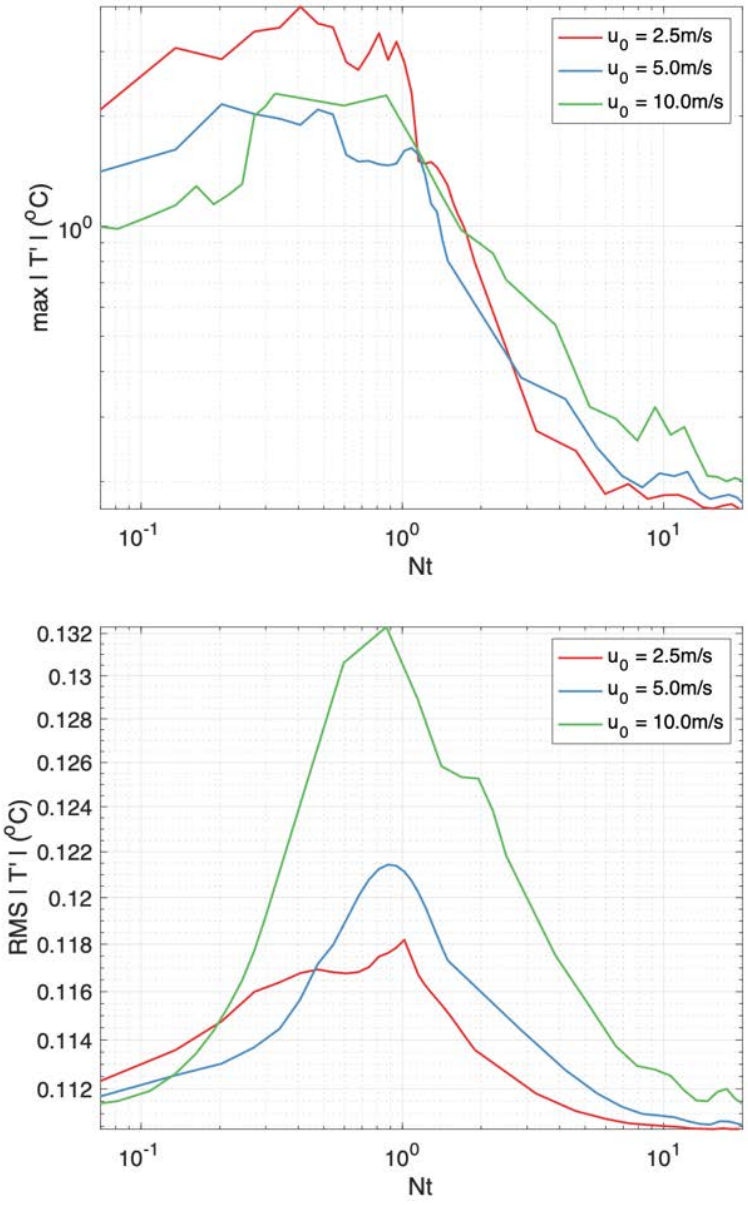

Figure 5. The top plot shows the maximum $|T'|$ as a function of non-dimensional time, *Nt*, while the bottom plot compares the RMS $|T'|$ as a function of non-dimensional time for various u_0

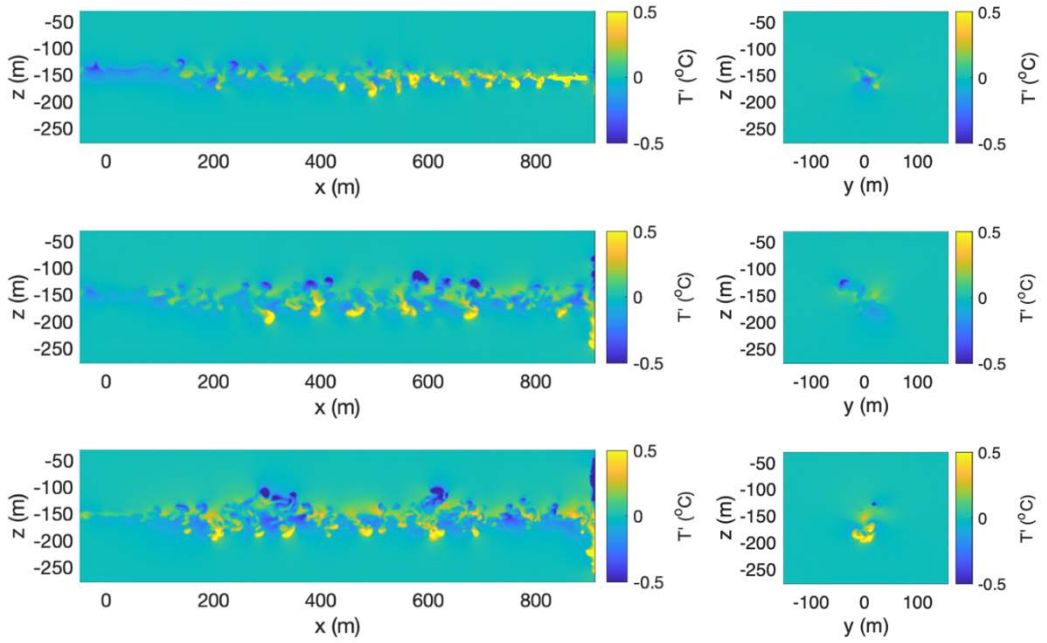

Figure 6. The left column shows the *xz*-plane while the right column shows the *yz*-plane through the entire domain taken at $y = 100$ and $x = 500$, respectively. The top, middle and bottom row are for u_0 of 2.5m/s, 5.0m/s and 10.0m/s, respectively, observed at $Nt \sim 1$.

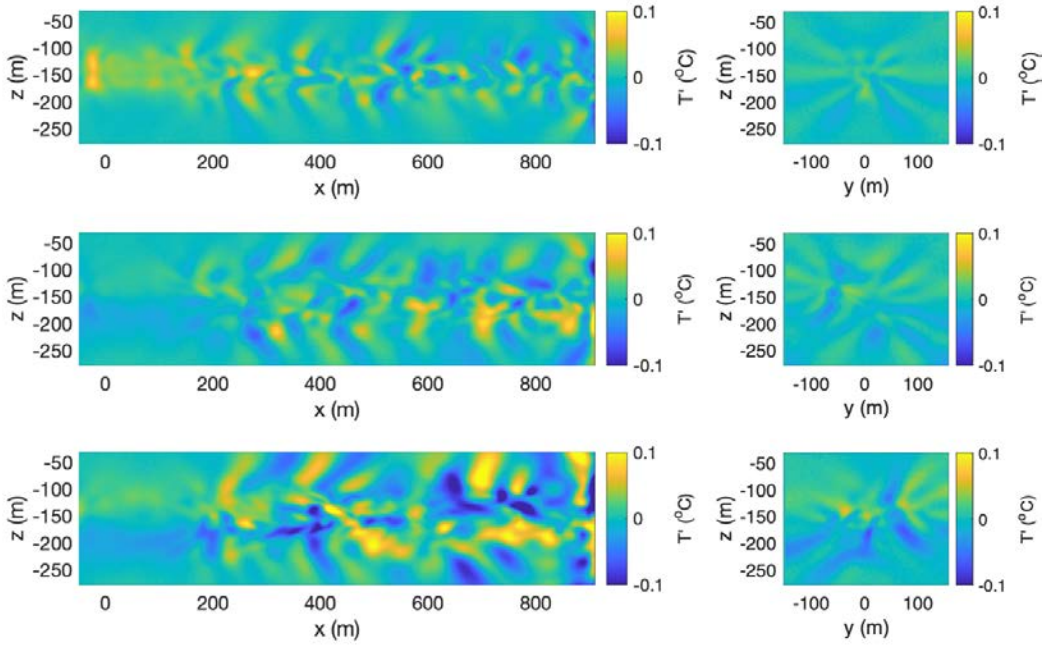

Figure 7. The left column shows the *xz*-plane while the right column shows the *yz*-plane through the entire domain taken at $y = 100$ and $x = 500$, respectively. The top, middle and bottom rows are for u_0 of 2.5m/s, 5.0m/s and 10.0m/s, respectively, observed at $Nt \sim 5$.

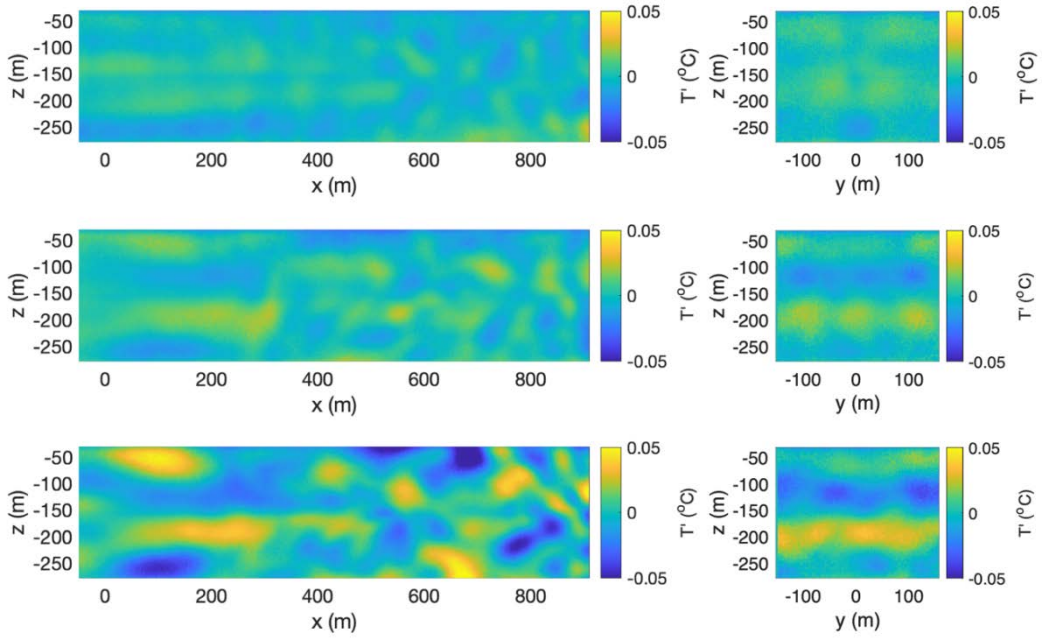

Figure 8. The left column shows the *xz*-plane while the right column shows the *yz*-plane through the entire domain taken at $y = 100$ and $x = 500$, respectively. The top, middle and bottom rows are for u_0 of 2.5m/s, 5.0m/s and 10.0m/s, respectively, observed at $Nt \sim 20$.

3. Background Salinity Field

The last control parameter varied in these simulations was the background salinity gradient. While $\frac{\partial \bar{S}}{\partial z}$ was varied for the runs, $\frac{\partial \bar{T}}{\partial z}$ was also changed in order to keep the background density, $\frac{\partial \bar{\rho}}{\partial z}$, constant. The background density gradient is defined as

$$\frac{\partial \bar{\rho}}{\partial z} = \rho_o \left(\beta \frac{\partial \bar{S}}{\partial z} - \alpha \frac{\partial \bar{T}}{\partial z} \right). \qquad (3.1)$$

For example, in the case with zero salinity gradient, $\frac{\partial \bar{T}}{\partial z}$ was reduced to 0.00375 °C /m. The values of u_0 and Q were held constant at 5.0m/s and 1.1×10^9W, respectively. In Figure 9, we plot the maximum $|T'|$ as well as the RMS of $|T'|$ as functions of non-dimensional time for these simulations. Since density is determined by temperature and salinity, heating the wake may change the level of neutral buoyancy in the system, but we don't see any obvious indications that this is the case in our simulations. The case with the largest salinity gradient

has the highest peak in the maximum $|T'|$ in this set of simulations. This observation of stronger thermal perturbation is due the fact that higher $\frac{\partial \bar{S}}{\partial z}$ will have a larger $\frac{\partial \bar{T}}{\partial z}$ in order to keep $\frac{\partial \bar{\rho}}{\partial z}$ constant, so the same amount of turbulent mixing would result in larger temperature perturbations. We also see a nearly opposite behavior in the maximum $|T'|$ plot as compared to the varying *Q* cases. Here, after the SB leaves the domain, there is still a re-adjustment phase, but the three cases take on very different values of $|T'|$ by $Nt \sim 1$ (whereas for different *Q*, they adjust to the same value). The low $\frac{\partial \bar{S}}{\partial z}$ case behaves comparably to our high *Q* case and vice versa, with T' for the low $\frac{\partial \bar{S}}{\partial z}$ case decreasing between $Nt \sim 0.25$ and $Nt \sim 1$. This could be connected to the temperature perturbations being effectively larger, while the SB is providing the same amount of heat in each case. It suggests that the significance of the heating is effectively moderated by the thermal stratification, which seems to set the value of the maximum T' at $Nt \sim 1$.

In Figure 10, we examine the thermal perturbation approximately twenty-five minutes later ($Nt \sim 5$). We observe that the wake core for the case with no salinity gradient is weaker than that of the other two cases. Other than that, there is not much significant difference between the morphology of the three simulations besides the larger thermal perturbations with stronger $\frac{\partial \bar{S}}{\partial z}$. Hypothetically, changing the salinity gradient would change the level of neutral buoyancy; however, we find no notable evidence of this in our simulations. Finally, we note that—particularly at late times—the presence of internal waves masks most thermal signatures, and thus we turn to a different metric to characterize the turbulent core of the wake.

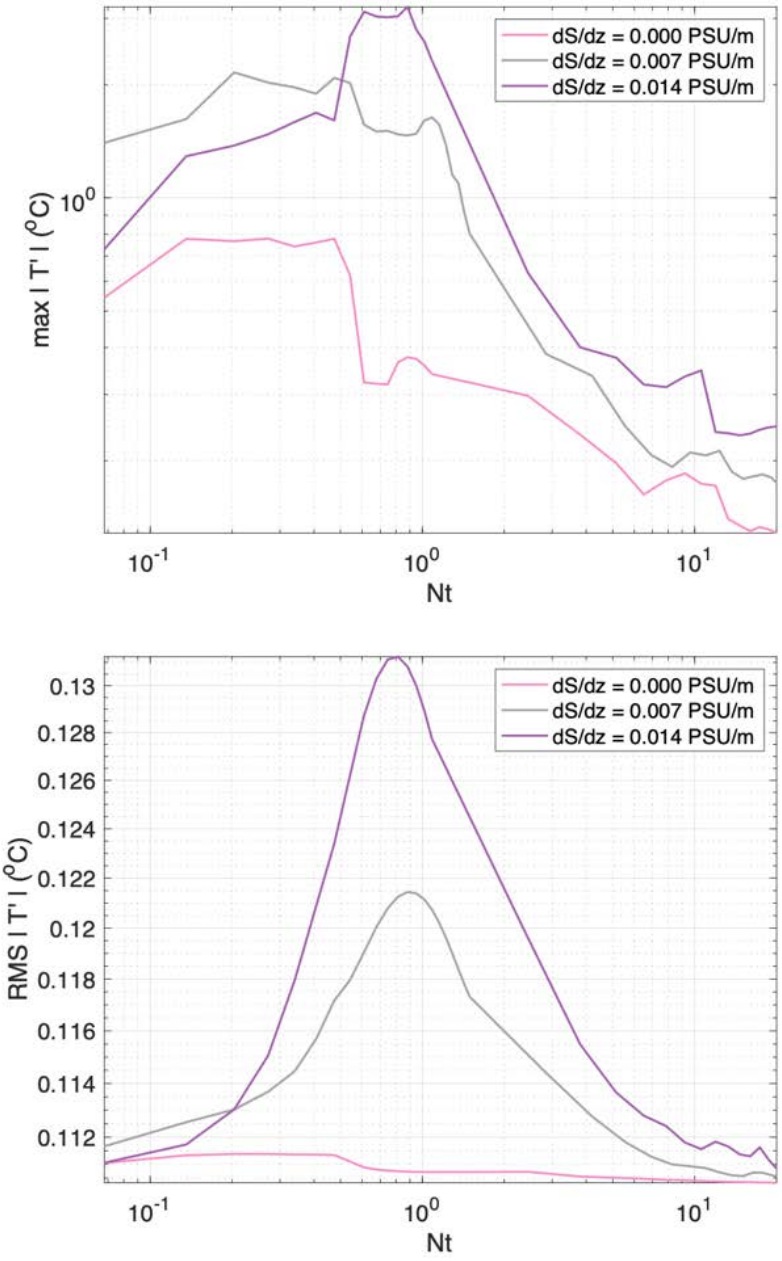

Figure 9. The top plot shows the maximum $|T'|$ as a function of non-dimensional time, *Nt*, while the bottom plot compares the RMS $|T'|$ as a function of non-dimensional time for various $\frac{\partial \bar{s}}{\partial z}$ runs.

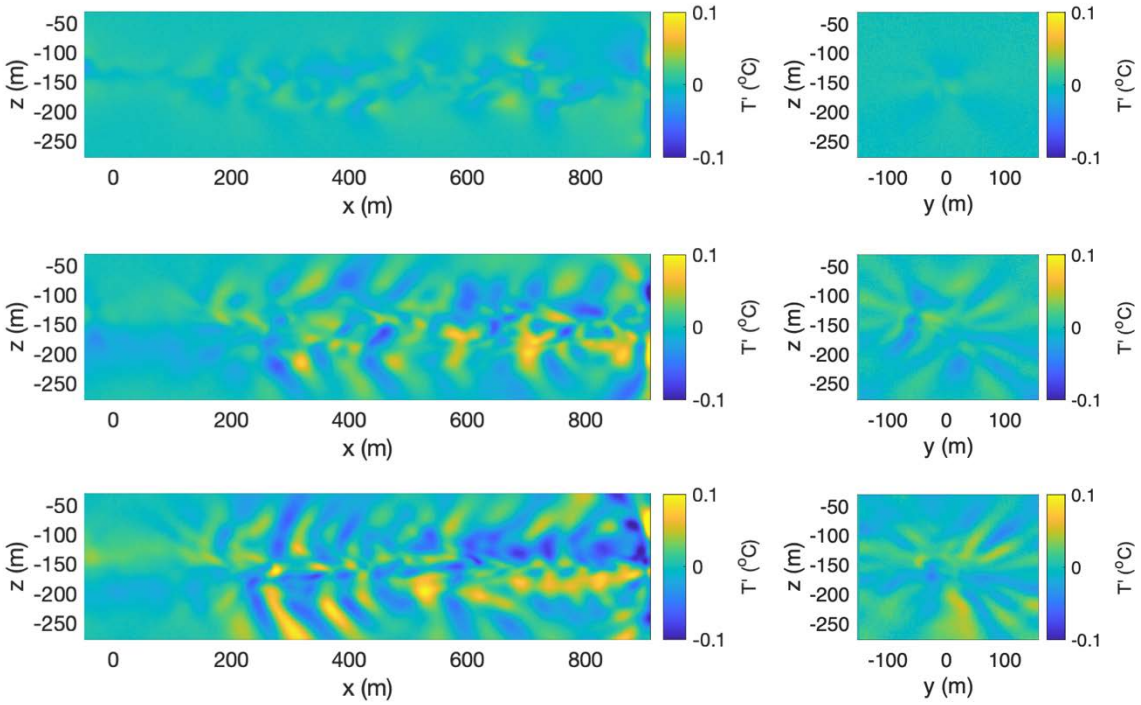

Figure 10. The left column shows the *xz*-plane while the right column shows the *yz*-plane through the entire domain taken at y = 100 and x = 500, respectively. The top, middle and bottom rows are for $\frac{\partial \bar{s}}{\partial z}$ of 0.000 PSU/m, 0.007 PSU/m and 0.014 PSU/m, respectively, observed at $Nt \sim 5$

B. DISSIPATION RATES

Other than using the thermal perturbation to characterize the structure of the wake, we also use the dissipation rate of turbulent kinetic energy, ε, to focus on the dynamics of the turbulent wake core. This quantity is frequently used as a measure of turbulence and is likely to highlight small-scale velocity features in the wake. Current oceanographic instruments are able to measure this quantity with an instrument sensitivity of 10^{-10}m^2/s^3 in the ocean; however, the ambient turbulent dissipation in the ocean was shown by Waterhouse et al., (2014) to be within the range of 10^{-10}–10^{-8}m^2 /s^3 (Waterhouse et al., 2014). The turbulent dissipation is defined as

$$\varepsilon = \upsilon \left[\left(\frac{\partial \boldsymbol{u}}{\partial x}\right)^2 + \left(\frac{\partial \boldsymbol{u}}{\partial y}\right)^2 + \left(\frac{\partial \boldsymbol{u}}{\partial z}\right)^2 \right]. \qquad (3.2)$$

Figure 11 shows the turbulent dissipation rate from the set of simulations with varying Q averaged along the path of the SB from $x = 150\text{m}$ to $x = 810\text{m}$. We can characterize the height and width of the wake by measuring the extent in y and z for which the x-averaged value of the turbulent dissipation rate exceeds half the maximum. At early times ($Nt \sim 1$), the turbulent dissipation rate shows the initial turbulent plumes caused by the immediate mixing of the sub. At $Nt \sim 5$, we observe that for all three cases, the finite-ε region can be considered to be well defined with the vertical extent varying from 40 to 60m. Horizontally, this region in all three cases extends horizontally from 80 to 100m, with the width of the wake generally increasing with Q, though this effect is slight. We observe that the vertical extent of the region with high ε for all three cases decreases between $Nt \sim 1$ and $Nt \sim 5$. In Figure 12, we show a slice of the turbulent dissipation rate taken at $x = 500\text{m}$ for $Nt \sim 5$ and 20. We observe the presence of a distinctive ε loop structure which persists at higher Re and at late times. This suggests that this feature has both temporal longevity and spatial coherence, which may allow for easy identification of submarine wakes in the ocean even up to the late wake. We suspect that the loop structure could be due to the presence of a core of mixed material that is surrounded by quiescent fluid, and the turbulent dissipation rate (as a derivative quantity) highlights that abrupt change from a turbulent region to a smooth region.

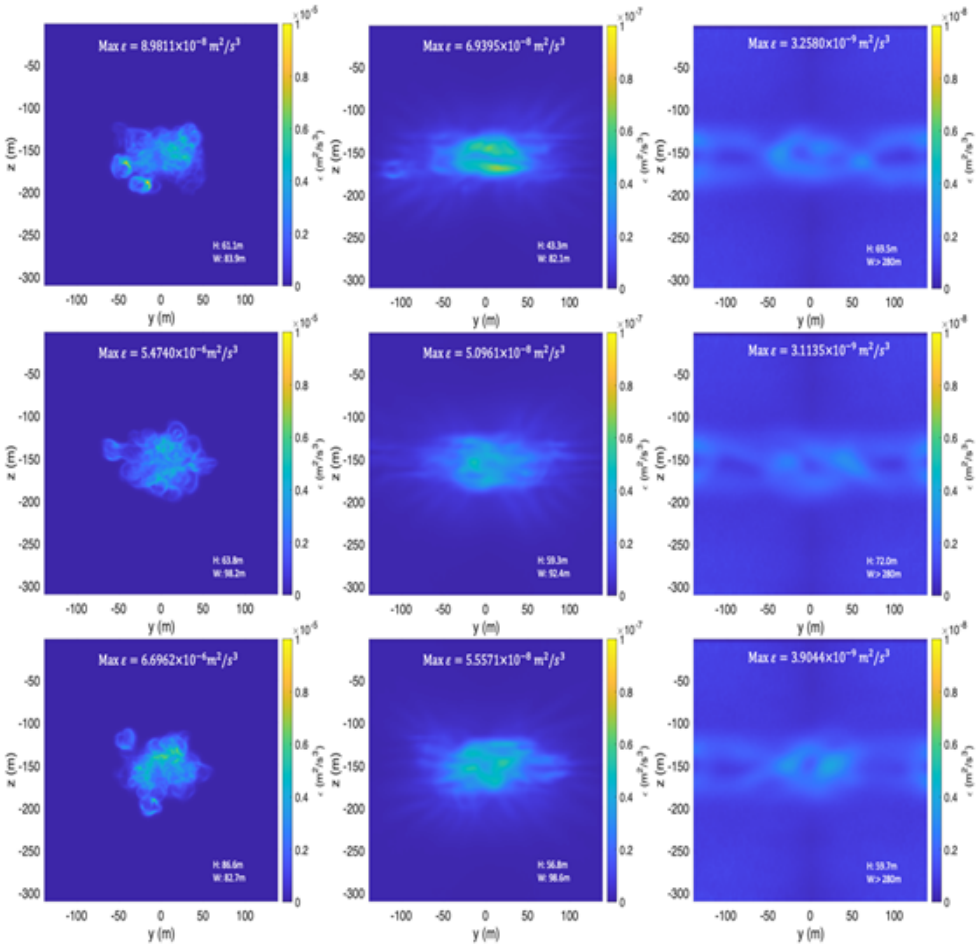

Figure 11. The left, middle and right column show the x-averaged ε taken at $Nt \sim 1$, 5, and 20, respectively. The top, middle and bottom rows are for Q of 0W, 2.2×10^9W and 4.4×10^9W, respectively. The height and width of the region with elevated ε is shown in bottom right of each plot.

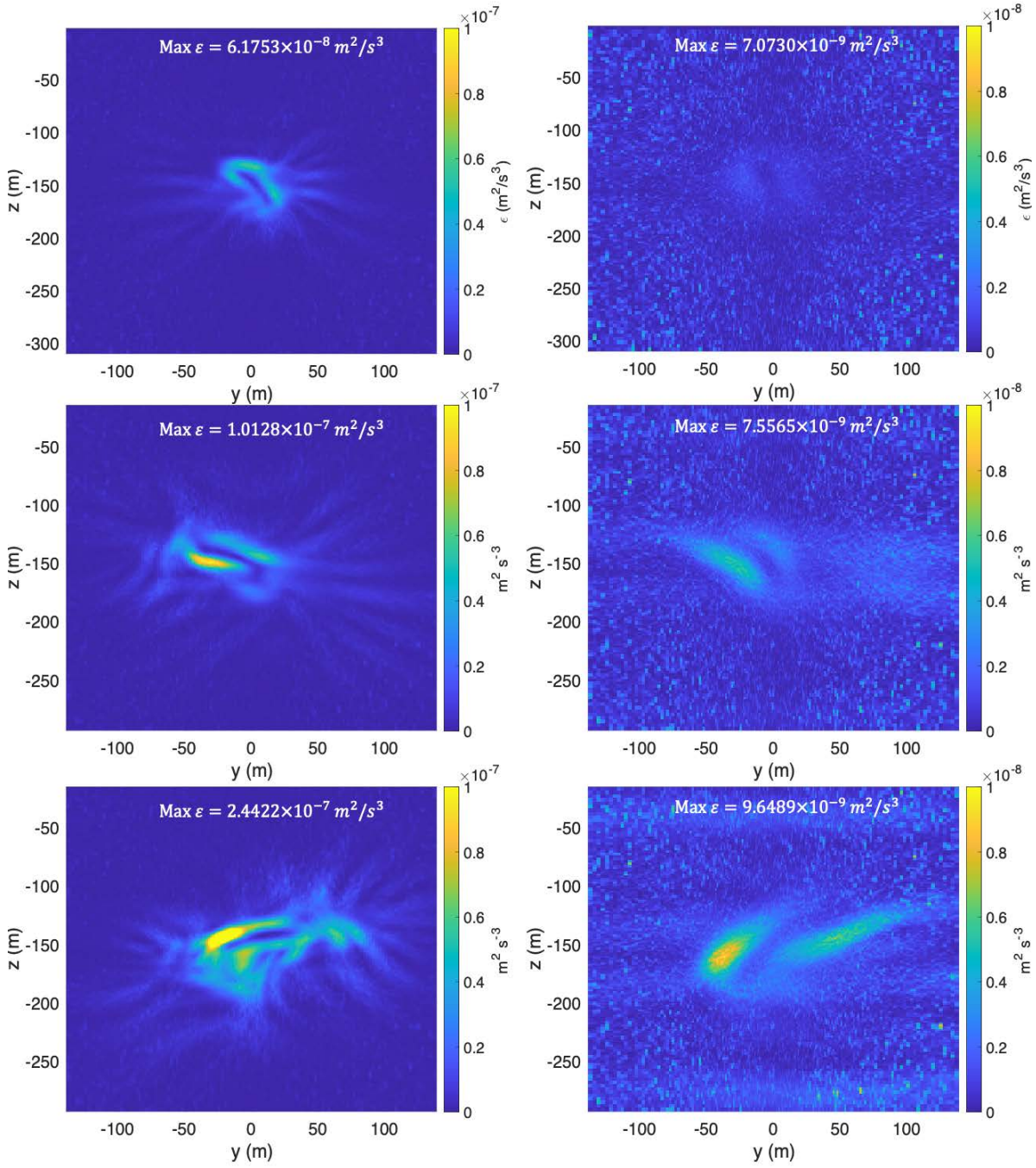

Figure 12. The left and right column show slices of ε taken at $Nt \sim 5$, and 20, respectively. The top, middle and bottom rows are for Q of 0W, 2.2×10^9W and 4.4×10^9W, respectively.

Figure 13 depicts the x-averaged ε from the set of simulations with varying u_0. By $Nt \sim 5$, the simulations with the largest SB velocities tend to generate the strongest wakes, which are also more extended in the vertical and horizontal directions. This is likely due to increased turbulent mixing of momentum in the immediate region behind the body. At $Nt \sim 20$, the maximum value of ε is observed to be the smallest for the case of $u_0 = 2.5$m/s, but it is still well within the detection threshold of present oceanographic instruments. However, the signal may be difficult to measure in the ocean due to background noise. We also observe a distinctive loop ε structure at late times for the case of slower speed. This could possibly be due to the weaker turbulence as a result of lower Re, hence preserving the structure of the wake more adequately. In all cases, the turbulent dissipation rate is above the detection threshold.

In Figure 14, we examine the results of the set of simulations with varying $\frac{\partial \bar{S}}{\partial z}$. At $Nt \sim 5$, we observe that for the case of $\frac{\partial \bar{S}}{\partial z}$ = 0.000 PSU/m, the persistent structures of the turbulent plumes (for example, see the $Nt \sim 1$ slices from Figure 11) can still be seen. Between the cases of $\frac{\partial \bar{S}}{\partial z}$ = 0.007 PSU/m and 0.014 PSU/m, we observe a larger max ε in the case of larger salinity gradient as the flattening of the wake is stronger, thus concentrating the turbulence to a smaller region. At $Nt \sim 20$, we observe loop ε structures in all three case with the higher salinity giving a more distinctive form. We could attribute this to the weaker gradients permitting less diffusion of temperature and salinity, hence preserving the buoyancy of plumes for greater distances. The characteristic loop structure is present in the higher salinity cases even in the mean epsilon field, which suggests that this structure's is temporally and spatially coherent over large scales. From these three simulations, it appears that salinity affects the structural form of the wake from the early to late stage, with stronger gradients resulting in greater coherence in the structure of turbulence.

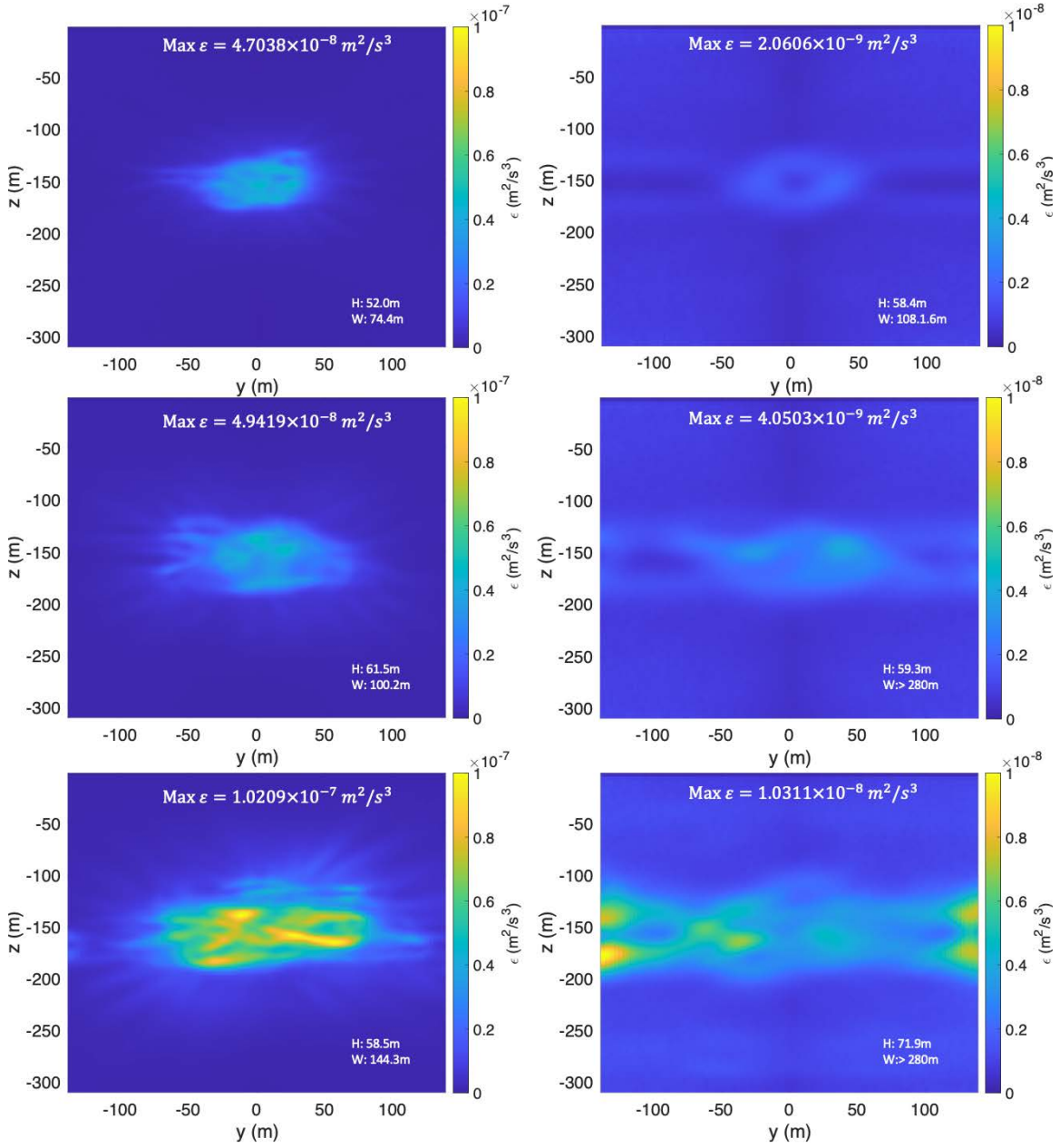

Figure 13. The left and right column show the ε taken at $Nt \sim 5$ and $Nt \sim 20$, respectively. The top, middle and bottom rows are for u_0 of 2.5m/s, 5.0m/s and 10m/s, respectively. The height and width of the area with elevated ε is shown in bottom right of each plot.

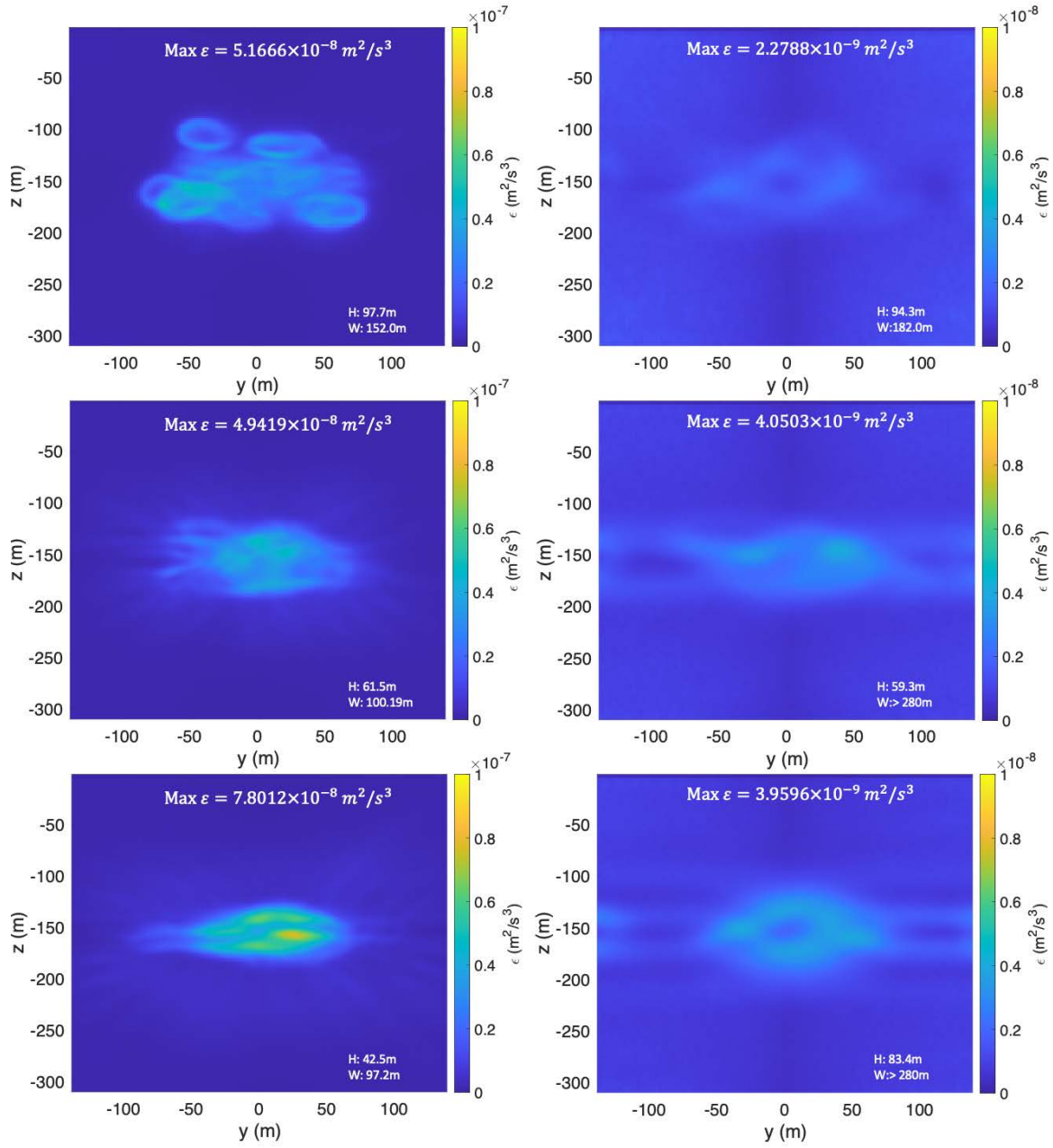

Figure 14. The left and right column show the ε taken at Nt ~ 5 and Nt ~ 20, respectively. The top, middle and bottom rows are for $\frac{\partial \bar{s}}{\partial z}$ of 0.000 PSU/m, 0.007 PSU/m and 0.014 PSU/m, respectively. The height and width of the area with high ε is shown in bottom right of each plot.

IV. DISCUSSION

A. CONCLUSION

This study presents the systematic analysis of wake signatures of a towed spherical SB with a heating source. We explore how the wake is affected by the physical properties of the SB, such as velocity and heating rate as well as the environmental parameters such as the salinity gradient. Based on a series of high-resolution numerical experiments, we draw four main conclusions.

Firstly, there were observable difference in the thermal perturbation of the wake between cases with and without heating for $Nt < 0.6$ (near wake). In all cases, the thermal perturbation plateaus upon SB exiting the domain at $Nt \sim 0.25$. By $Nt \sim 1$, the thermal perturbations were eased as a result of the wake's warm region rising to the level of neutral buoyancy combined with the effect of turbulent mixing. Beyond $Nt \sim 1$, there was no observable influence of heating on the thermal and turbulent features of the wake.

Secondly, the temperature perturbation of the heated wake has a strong dependence on the velocity of the SB. At $Nt < 1$, a higher maximum temperature perturbation was observed for the slower case as a result of a reduced amount of turbulence in contrast to the other two cases. This eventually led to less mixing in the SB wake. This reduced amount of turbulence resulted in the lowest RMS temperature perturbation for the slowest case. Hence, we can deduce that a slower SB would result in a higher detection rate when using temperature anomaly at the earliest stages of the wake. However, the wake loses its detectable signatures more rapidly than in the case for a faster SB. Comparing the wake structures between the varying speeds, we also observed that heating only affected the wake at the early stages. The Reynolds number was observed to play a more important part in determining the wake dynamics.

Thirdly, a larger salinity gradient resulted in a higher maximum temperature perturbation. We observed that the maximum temperature perturbation took on very different values at $Nt > 1$ in all three cases. The low salinity gradient case behaved somewhat similar to the case of higher heating and vice versa. At $Nt \sim 1$, we observed

different values of thermal perturbation which could possibly be due to the result of thermal stratification mitigating the effect of heating. We expected that changes in the salinity gradient would adjust the level of neutral buoyancy; however, we were not able to find support of this in our simulations.

Lastly, when we examined the turbulent dissipation of our simulations, we observed a distinctive turbulent dissipation loop structure in all cases at $Nt \geq 5$. This loop structure could be due to the presence of quiescent fluid enclosing a core of mixed material. The sudden change from a turbulent region to a smooth region is evident from the turbulent dissipation rate. This pattern could only be seen in the late stage of the slower velocity case possibly due to the weaker turbulence caused due to lower Reynolds number. The structure of wake turbulence becomes more pronounced in experiments performed with higher salinity gradient. Both temporal longevity and spatial coherence of the distinctive patterns of kinetic energy dissipation may be utilized in the development of hydrodynamic algorithms for identification of submarine wakes in the ocean.

B. OPERATIONAL RELEVANCE

Understanding how heated wake structures behave will significantly enhance Anti-Submarine Warfare (ASW) since submarines inevitably produce such flow patterns when propagating through the stratified ocean, and these wakes may persist for hours. The temperature perturbation field of heated wake can used to determine the past locations of submarines using networks of ASW sensors. These sensors include sonar buoys and unmanned underwater vehicles which are capable collecting temperature field required for analysis. The insights from this study can be used to improve the existing hydrodynamic detection algorithms and to develop new approaches. Beside the temperature perturbation field, the turbulence dissipation rate has also shown to be an easily identifiable feature to determine the presence of a late wake by a submerged body. In order to calculate turbulence dissipation rate in the ocean, the method of collecting the three-dimensional temperature and velocity gradients will require further steps. One of the most common way to resolve them would be to measure the gradient in one dimension and thereafter apply approximation three-dimensionally assuming isotropy and incompressibility. The analysis

of the dissipation rate and/or other microstructure signatures will make it possible to more accurately and reliably determine the wake location and hence better track the adversarial submarines.

C. FUTURE RESEARCH

This work opens up avenues for a number of future research topics in the field of stratified wakes. One such possibility is the use of a real-life setup using a REMUS Autonomous Underwater Vehicle affixed with a heater to generate a warm wake and following it with CTP sensors to capture the temperature perturbation and turbulent dissipation of the stratified water column. This research would be able to validate the results captured in this study. To further improve on the realism of this model, the sphere could be replaced by an object more representative of submarines or unmanned underwater vehicles. This study's findings on the effect of heated wakes are merely the foundation for future DNS investigations that will incorporate the effects of acceleration, deceleration, and turning.

THIS PAGE INTENTIONALLY LEFT BLANK

LIST OF REFERENCES

Fiekas, H. V., 1997: Experimental Investigations Inside the Turbulent Wake of a Submerged Submarine. UDT, 97 pp.

Hopfinger, E. J., J.-B. Flor J.-M. Chomaz, and P. Bonneton, 1991: Internal waves generated by a moving sphere and its wake in a stratified fluid. *Exp. Fluids*, **11**, 255–261.

Lin, J. T., and Y.H. Pao, 1979: Wakes in stratified fluid. *Annu. Rev. Fluid Mechanics*, **11**, 317–338.

Marshall, J., C. Hill, L. Perelman, and A. Adcroft, 1997: Hydrostatic, quasi-hydrostatic, and nonhydrostatic ocean modeling. *J. Geophys. Res.: Oceans*, **102**, 5733–5752.

Schooley, A.H., and R.W. Stewart, 1963: Experiments with a self-propelled body submerged in a fluid with a vertical density gradient. *J. Fluid Mech*. **15**, 83–96.

Spedding, G.R., 1997: The evolution of initially turbulent bluff-body wakes at high internal Froude number. *J. Fluid Mech*. **337**, 283–301.

Voropayev, S. I., G.B. McEachern, H.J.S. Fernando, and D.L. Boyer, 1999: Large vortex structures behind a maneuvering body in stratified fluids. *Phys. Fluids*, **11**, 1682–1684, https://doi.org/10.1063/1.870030.

Waterhouse, A. F., and Coauthors, 2014: Global Patterns of Diapycnal Mixing from Measurements of the Turbulent Dissipation Rate. J. Phys. Oceanogr. **44**,1854–1872, https://doi.org/10.1175/JPO-D-13-0104.1.

Zhang, X., L. Guo, R. Hu, and C. Liu, 2019: Cold-thermal wake characteristics of submarine in temperature-density stratified seawater. Proc. SPIE 11023, *Fifth Symposium on Novel Optoelectronic Detection Technology and Application*, Xi'an, China, https://doi.org/10.1117/12.2521927.

THIS PAGE INTENTIONALLY LEFT BLANK

INITIAL DISTRIBUTION LIST

1. Defense Technical Information Center
   Ft. Belvoir, Virginia

2. Dudley Knox Library
   Naval Postgraduate School
   Monterey, California